Transient wave propagation in a 1-D gradient model with material nonlinearity

Fărăgău, Andrei B.; Hollm, Marten ; Dostal, Leo; Metrikine, Andrei V.; van Dalen, Karel N.

DOI
10.1016/j.euromechsol.2024.105543

Publication date
2024

Document Version
Final published version

Published in
European Journal of Mechanics A - Solids

European Journal of Mechanics / A Solids 111 (2025) 105543

Contents lists available at ScienceDirect

European Journal of Mechanics / A Solids

journal homepage: www.elsevier.com/locate/ejmsol

Full length article

Transient wave propagation in a 1-D gradient model with material nonlinearity

Andrei B. Fărăgău [a,*], Marten Hollm [b], Leo Dostal [b], Andrei V. Metrikine [a], Karel N. van Dalen [a]

[a] Faculty of Civil Engineering and Geosciences, Delft University of Technology, Stevinweg 1, 2628 CN Delft, Netherlands
[b] Institute of Mechanics and Ocean Engineering, Hamburg University of Technology, Eissendorfer Strasse 42, 21073 Hamburg, Germany

ARTICLE INFO

Keywords:
Gradient elasticity
Nonlinear continuum
Nonlinear wave propagation
Soil dynamics
Softening material
Seismic site response

ABSTRACT

A novel nonlinear 1-D gradient model has been previously proposed by the authors, combining (i) the higher-order gradient terms that capture the influence of material micro-structure and (ii) a nonlinear softening material behavior through the use of a hyperbolic constitutive model. While the previous study focused on the existence and properties of solitary-type waves, the current study focuses on the characteristics of the transient wave propagation in the proposed model. Findings show that as nonlinearity increases, the bulk of the wave slows down, and its shape becomes more distorted in comparison to the response of the linear system. The energy analysis reveals that, unlike the linear system, the nonlinear one continuously exchanges energy, in which the kinetic energy decreases over time while the potential one increases. Furthermore, the spectral (wavenumber) energy density of the nonlinear-*elastic* system presents peaks at large wavenumbers. However, these are eliminated when a small amount of linear viscous damping is added indicating that they are not physically relevant. A notable feature that persists despite the presence of damping is the formation of small-amplitude waves traveling in the opposite direction to the main wave. Generalized continua, like gradient elasticity models, miss the small energy scatter by the micro-structure. This study shows that adding material nonlinearity to a homogeneous generalized continuum can capture reverse energy propagation, though at much smaller magnitudes than the main wave. These findings shed light on the characteristics of the transient wave propagation predicted by the proposed nonlinear 1-D gradient model and its applicability in, for example, predicting the seismic site response.

1. Introduction

Researchers have developed gradient elasticity models, also known as higher-order gradient continua or micro-structured solids, to effectively capture small (sub-wavelength) scale material heterogeneity without modeling it explicitly. Unlike classical continua, these models incorporate higher-order gradient terms (and even higher-order fractional derivatives Tarasov and Aifantis, 2015; Patnaik et al., 2021) in the stress–strain relation to account for micro-structural effects (Gusev and Lurie, 2017; Zhou et al., 2016; Abali et al., 2017; Polizzotto, 2017; Lurie et al., 2021; Dell'isola and Steigmann, 2020), maintaining a homogeneous material description. This approach introduces dispersive effects, especially for shorter waves (Mindlin, 1964; Vardoulakis and Aifantis, 1994; Rubin et al., 1995; Mühlhaus and Oka, 1996; Geers et al., 2001; Andrianov et al., 2011; Metrikine, 2006; Askes et al., 2008; Askes and Aifantis, 2011; Papargyri-Beskou et al., 2011), preventing the formation of jumps and yielding physically realizable solutions. These higher-order gradient terms are derived naturally using asymptotic homogenization techniques for periodically inhomogeneous media (Metrikine, 2006; Kouznetsova et al., 2002; Fish et al., 2002; Andrianov et al., 2008; Craster et al., 2010; Capdeville et al., 2010; Gómez-Silva and Zaera, 2023; Pirmoradi et al., 2024). For a comprehensive overview of the development of gradient elasticity models, we refer to Askes and Aifantis (2011).

Gradient elasticity models can be generally employed when micro-structural (i.e., sub-wavelength) effects considerably influence the mechanical behavior of materials (Metrikine and Askes, 2002), and when modeling the sub-wavelength heterogeneity (e.g., de Oliveira Barbosa et al. (2021, 2022) and Fărăgău et al. (2022)) is undesirable. Examples include capturing wave dispersion in granular materials (Altan and Aifantis, 1997; Chang and Gao, 1995; Suiker et al., 2001; Mühlhaus and Oka, 1996), capturing micro-structural effects near crack tips (Huang et al., 1997; Gourgiotis and Georgiadis, 2009; Castelluccio et al., 2021), modeling the behavior of woven fabrics (Dell'Isola and Steigmann, 2015), and in describing softening phenomena (Triantafyllidis and

* Corresponding author.
E-mail address: A.B.Faragau@tudelft.nl (A.B. Fărăgău).

https://doi.org/10.1016/j.euromechsol.2024.105543
Received 1 September 2024; Received in revised form 14 November 2024; Accepted 17 December 2024
Available online 25 December 2024

Aifantis, 1986; Aifantis, 1987; Peerlings et al., 1996; Schreyer and Chen, 1986; Lasry and Belytschko, 1988; Sluys and de Borst, 1992). More recently, gradient elasticity models have been used in the realm of micro- and nano-technology (Behnam-Rasouli et al., 2024; Anicode et al., 2024; Podulka and Macek, 2024; Liebold and Müller, 2016; Nguyen et al., 2019; Gómez-Silva and Askes, 2024).

An area of research where both small-scale heterogeneity and material softening play a significant role is soil dynamics, particularly in earthquake engineering and seismic site response forecasting. Soil exhibits clear heterogeneity at different scales and, thus, the definition of small-scale heterogeneity varies with the wavelength of interest. For long seismic waves, it may refer to different sediment layers, while for shorter waves, it can indicate particle contacts and pores in the soil. This study focuses on seismic waves, where small-scale heterogeneity pertains to sediment layers with varying properties. It is also well known that soil stiffness decreases with increased strain, a behavior extensively described in the geotechnical community using the hyperbolic soil model (Hardin and Drnevich, 1972; Kramer, 1996), which represents a non-polynomial type of nonlinearity. Although these characteristics have been studied separately—using *linear* gradient elasticity models to capture soil micro-structure and classical continua with the hyperbolic material model to investigate softening behavior and superharmonic resonances (Zhang et al., 2021)—studies that consider them simultaneously are scarce. Some studies did consider geometrically nonlinear gradient elasticity models (e.g., Torabi et al. (2021), Tran and Niiranen (2020), Ma et al. (2022) and Wazne et al. (2024)), but not material nonlinearity. Gholami et al. (2020) considered material nonlinearity in the context of gradient elasticity, but the models considered were of finite extent and wave propagation was not investigated.

To address the knowledge gap in the fundamental nonlinear dynamics of seismic site response, the authors previously introduced a novel 1-D gradient model for nonlinear seismic wave predictions (Dostal et al., 2022). This model integrates (i) higher-order gradient terms that account for small-scale soil heterogeneity and (ii) nonlinear softening soil behavior using the hyperbolic soil model. The model was designed to represent bulk shear waves propagating in soil; however, its general formulation is applicable to other scenarios where micro-structure and material softening nonlinearity play a significant role. While the research in Ref. Dostal et al. (2022) focused on the existence of localized *stationary*-type waves, the current study focuses on the *transient* wave propagation. Specifically, this study examines changes in response with varying levels of nonlinearity (Section 5), energy redistribution over wavenumbers and its temporal evolution (Section 6), the evolution of kinetic and potential energy over time (Section 6), and the formation of small-amplitude waves traveling in the direction opposite to the main wave (Section 7).

Regarding the last aspect, generalized continua (such as gradient elasticity models) can accurately predict the effects of heterogeneity only for spatial scales that are several times larger than the characteristic scale of heterogeneity. Consequently, the small amount of energy caused by scattering from small-scale heterogeneity, which propagates in the opposite direction of the main wave, cannot be captured in linear generalized continua. This article demonstrates that introducing material nonlinearity in such a homogeneous generalized continuum can capture energy propagation in the opposite direction (though it is orders of magnitude smaller than the main wave). To the best of the authors' knowledge, this is the first time this has been reported.

2. Model, solution method, and response example

2.1. Model

As mentioned in the introduction, the *nonlinear* gradient model first proposed by Dostal et al. (2022) comprises two well-established models: (i) a 1-D gradient model that captures the effects of micro-structure, and (ii) a nonlinear constitutive model that describes material softening with increased strain. Specifically, the latter uses the hyperbolic soil model (Hardin and Drnevich, 1972; Kramer, 1996), where the (secant) shear modulus G depends on the representative shear strain γ through a non-polynomial relation, as follows:

$$G(\gamma) = \frac{G_0}{1 + \left(\gamma/\gamma_{\text{ref}}\right)^{\beta}}, \tag{1}$$

where G_0 is the small-strain shear modulus while γ_{ref} and β are material constants (Hardin and Drnevich, 1972; Kramer, 1996). It must be emphasized that although this hyperbolic softening material behavior was introduced in Ref. Dostal et al. (2022) to characterize soil, it can be representative of a more general class of materials that exhibit a softening behavior. The nonlinear material model used in this study does not include plasticity and is therefore suitable for small to medium–large strain levels, but unsuitable for extremely large ones.

Table 1
Medium parameter values.

G_0 [Pa]	ρ [kg m^{-3}]	β [–]	γ_{ref} [–]	B_1 [–]	B_2 [–]	L [m]	η [s]
$111.86 \cdot 10^6$	2009.8	0.91	10^{-3}	1	1.78	0.2	5×10^{-5}

The equation of motion of the nonlinear 1-D gradient model employed in this study reads (Dostal et al., 2022)

$$\rho \frac{\partial^2 u}{\partial t^2} = \frac{\partial}{\partial z}\left(G(\gamma)\frac{\partial u}{\partial z} - B_1 L^2 \frac{\partial^2}{\partial z^2}\left(G(\gamma)\frac{\partial u}{\partial z}\right) + B_2 \frac{\rho L^2}{G_0}\frac{\partial^2}{\partial t^2}\left(G(\gamma)\frac{\partial u}{\partial z}\right)\right) + G_0 \eta \frac{\partial^3 u}{\partial t \partial z^2}, \tag{2}$$

where ρ is the mass density of soil, B_1, B_2 are dimensionless constants, L is the characteristic length of the soil micro-structure, z and t denote space and time, respectively, and u is the soil displacement. For some soil displacement $u(z,t)$, the corresponding strain $\gamma(z,t)$ is given by $\gamma(z,t) = \frac{\sqrt{3}}{2}\left|\frac{\partial u}{\partial z}\right|$, see Refs. Zhang et al. (2021) and Dostal et al. (2022). The model was developed to represent bulk shear wave propagation in soil, but its general formulation is also suitable for other cases where micro-structural effects and material softening nonlinearity are significant.

The gradient model obtained in the *linear-elastic* limit case (i.e., replacing $G(\gamma)$ by G_0 and neglecting damping in Eq. (2)) was derived before by Metrikine and Askes (2002) from a discrete model using a continualization procedure, and a similar equation was also employed by Georgiadis et al. (2000) to examine the existence of horizontally polarized surface waves.

Compared to the model presented in Dostal et al. (2022), Eq. (2) includes an additional linear viscous damping term with damping factor η incorporated to remove numerical noise and to verify if features observed in the system without damping persist when adding a very small amount of damping. It must be emphasized that throughout the work, a very small damping factor is used (see Table 1) such that it does not affect the results considerably. If not noted otherwise, the numerical values of G_0, ρ, β, γ_{ref}, B_1, B_3, L, and η given in Table 1 are used throughout this work. The values of G_0, ρ, β and γ_{ref} have been chosen to represent soil, and the values of the parameters related to the higher-order gradient terms are similar to the ones used in Metrikine (2006).

The system under consideration should ideally have an infinite spatial extent, but this is not feasible due to the discretization applied in the numerical solution method (see Section 2.2). Therefore, fixed boundary conditions are imposed at a sufficiently large distance to avoid introducing artifacts in the response. Furthermore, the system is subject to initial conditions, which are prescribed in this study as trivial initial displacement and non-zero initial velocity representing a spatial-derivative of the Gaussian pulse. The initial conditions read

$$u(z, t=0) = 0, \qquad \frac{\partial u}{\partial t}(z, t=0) = 2A\frac{z}{\sigma^2}\sqrt{\frac{G_0}{\rho}}\mathrm{e}^{-\frac{z^2}{2\sigma^2}}, \tag{3}$$

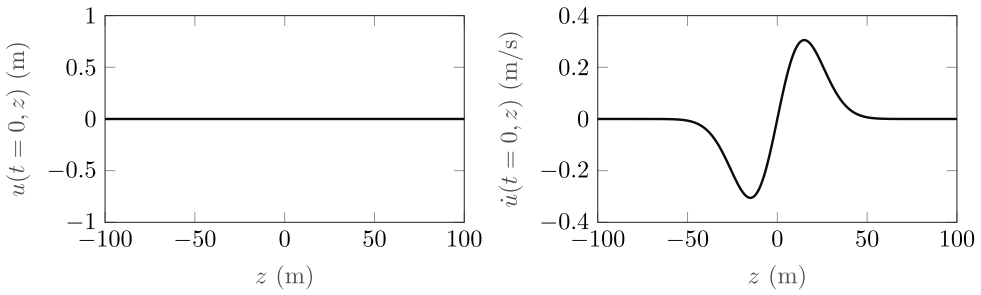

Fig. 1. Representation of the initial conditions used throughout the remainder of the study.

where A and σ are the amplitude and standard deviation of the Gaussian pulse, respectively. To aid the reader, Fig. 1 presents a visual representations of the initial conditions used throughout the remainder of the study. It must be emphasized that the solution method (Section 2.2) and the model characteristics described in this work (Sections 5–7) are not limited to this specific set of initial conditions.

2.2. Solution method

The response of the system is determined by solving Eq. (2) using a novel finite difference scheme, which has first been presented in Dostal et al. (2022) for the undamped case, i.e. $\eta = 0$ s. In this section, we extend the scheme by including the damping term $G_0\eta\frac{\partial^3 u}{\partial t\partial z^2}$.

It the following, it is assumed that the solution $u(z,t)$ of Eq. (2) exists in time $t \in [0, \mathbb{T}]$. Furthermore, the numerical solution is computed in space $z \in [Z_\ell, Z_h]$. Although a bounded spatial domain is considered, the infinite extent of the system will be ensured by choosing the values of Z_ℓ and Z_h such that the initial pulse cannot reach the boundaries in the finite simulation time of length $\mathbb{T}$.

To compute the solution $u(z,t)$ of Eq. (2) for $(t,z) \in [0,\mathbb{T}]\times[Z_\ell, Z_h]$, a grid in time

$$0 = t_0 < t_1 < \cdots < t_N = \mathbb{T}, \quad t_n = n\Delta t \ \text{ for } n = 0,\dots,N, \ \Delta t = \frac{\mathbb{T}}{N}, \tag{4}$$

and a grid in space

$$Z_\ell = z_0 < z_1 < \cdots < z_M = Z_h, \quad z_i = i\Delta z \ \text{ for } i = 0,\dots,M,$$
$$\Delta z = \frac{Z_\ell - Z_h}{M} \tag{5}$$

are introduced. Furthermore, in order to shorten the notation, $(\dots)_{,z}$ and $(\dots)_{,t}$ will denote the partial differentiation with respect to z and t in the following, respectively. The same notation is used to denote partial derivatives of higher order.

Using

$$h(u_{,z}) := G(u_{,z})\,u_{,z}, \tag{6}$$

Eq. (2) can be written as

$$\rho\,u_{,tt} = h_{,z} - B_1 L^2 h_{,zzz} + B_2\frac{\rho L^2}{G_0}h_{,tz} + G_0\eta\,u_{,tzz}. \tag{7}$$

Assuming that the solution is known at the timepoints t_{n-1} and t_n and replacing the time derivative by a finite-difference approximation, Eq. (7) results in the nonlinear equation

$$\mathbf{f}(\mathbf{u}^{n+1}) = \mathbf{0}, \tag{8}$$

with

$$\mathbf{u}^{n+1} := \left[u_0^{n+1}, u_1^{n+1}, \dots, u_M^{n+1}\right]^{\mathrm{T}}, \tag{9}$$

and

$$\begin{aligned} f_i(\mathbf{u}^{n+1}) :=& \rho\,\frac{u_i^{n+1} - 2u_i^n + u_i^{n-1}}{\Delta t^2} - \frac{h_{,z}(u_{i,z}^{n+1}) + 2h_{,z}(u_{i,z}^n) + h_{,z}(u_{i,z}^{n-1})}{4} \\ &+ B_1 L^2\,\frac{h_{,zzz}(u_{i,z}^{n+1}) + 2h_{,zzz}(u_{i,z}^n) + h_{,zzz}(u_{i,z}^{n-1})}{4} \\ &- B_2\frac{\rho L^2}{G_0}\,\frac{h_{,z}(u_{i,z}^{n+1}) - 2h_{,z}(u_{i,z}^n) + h_{,z}(u_{i,z}^{n-1})}{\Delta t^2} - G_0\eta\,\frac{u_{i,zz}^{n+1} - u_{i,zz}^{n-1}}{2\Delta t}. \end{aligned} \tag{10}$$

Here, f_i denotes the ith component of $\mathbf{f}$ and u_i^n is a grid function approximating the solution at time t_n and space z_i, i.e. $u_i^n \approx u(z_i,t_n)$. In the same way, $u_{i,z}^n$ and $u_{i,zz}^n$ approximate $u_{,z}(z_i,t_n)$ and $u_{,zz}(z_i,t_n)$, respectively. Eqs. (8) and (10) approximate Eq. (7) (evaluated at $t = t_n$) up to an accuracy of $\mathcal{O}(\Delta t^2)$, whereby $\mathcal{O}(\cdot)$ represents the big O notation.

Next, the space derivatives appearing in Eq. (10) have to be discretized. For this, standard finite-difference approximations in space are used, which have an accuracy of $\mathcal{O}(\Delta z^2)$. The corresponding finite-difference approximations of $u_{i,z}$, $u_{i,zz}$, $h_{,z}$, and $h_{,zzz}$ can be found in Appendix, Eqs. (A.1)–(A.4).

Since Eq. (8) is nonlinear, a numerical scheme has to be used to calculate u_i^{n+1} iteratively. For this, Newton's method is used, for which the computation of the Jacobian matrix is necessary. The entries of the Jacobian matrix can be computed analytically and are given in Appendix, Eq. (A.6). This concludes the numerical scheme for the computation of solutions to Eq. (2).

2.3. Response example

Fig. 2 illustrates a typical displacement response both in space and time. The system is subject to clamped boundary conditions at $z = \pm 1500$ m. However, the domain length is selected to ensure that waves do not interact with the boundaries during the entire simulation period, thus preventing unwanted boundary artifacts. The response exhibits two primary pulses propagating outward with opposite amplitudes, consistent with the applied initial conditions. As the response evolves, the shape of these main traveling pulses undergoes changes due to (i) material nonlinearity introduced by the strain-dependent shear modulus, and (ii) dispersion effects introduced by the higher-order terms.

3. Energy analysis

To offer a comprehensive picture of the solution behavior, we analyze the evolution of the kinetic, potential, and total energy of the system with time. These quantities as well as their wavenumber spectra are derived herein. Neglecting the dissipative term in Eq. (2), the energy balance reads

$$\frac{\partial E_{\mathrm{k}}}{\partial t} + \frac{\partial E_{\mathrm{p}}}{\partial t} = 0, \tag{11}$$

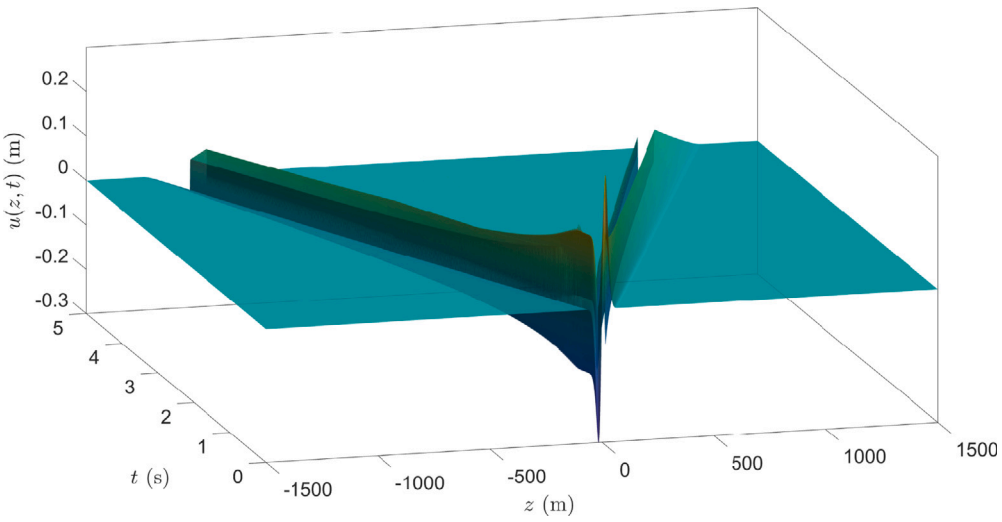

Fig. 2. The response (displacement) of the nonlinear system ($\gamma_{\text{ref}} = 0.001$) versus time and space.

where E_{k} and E_{p} represent the kinetic and potential energies, respectively. The first term in Eq. (11) reads

$$\frac{\partial E_{\text{k}}}{\partial t} = \frac{\partial}{\partial t}\int_{-\infty}^{\infty} \rho\left(\frac{\partial u}{\partial t}\right)^2 \text{d}z. \tag{12}$$

The second term in Eq. (11) has a slightly more complex expression and reads

$$\frac{\partial E_{\text{p}}}{\partial t} = \int_{-\infty}^{\infty} \frac{\partial^2 u}{\partial z \partial t}\sigma_{zx}\text{d}z = \frac{\partial}{\partial t}\int_{-\infty}^{\infty}\left(\int_0^t \frac{\partial^2 u(z,\tau)}{\partial z \partial \tau}\sigma_{zx}(z,\tau)\text{d}\tau + e_{\text{p}}(z,0)\right)\text{d}z, \tag{13}$$

$$\sigma_{zx} = G(\gamma)\frac{\partial u}{\partial z} - B_1 L^2 \frac{\partial^2}{\partial z^2}\left(G(\gamma)\frac{\partial u}{\partial z}\right) + B_2 \frac{\rho L^2}{G_0}\frac{\partial^2}{\partial t^2}\left(G(\gamma)\frac{\partial u}{\partial z}\right), \tag{14}$$

where σ_{zx} is the shear stress and $e_{\text{p}}(z,0)$ is the initial potential energy density. For the initial conditions given in Eq. (3), it holds that $e_{\text{p}}(z,0) = 0$.

The spectral energy densities can be derived by expressing the space-domain quantities appearing in Eqs. (12) and (13) as inverse-Fourier transforms of their Fourier-domain counterparts and manipulating the expressions as done in e.g. Refs. Vesnitskii and Metrikin (1996), van Dalen et al. (2015), Fărăgău et al. (2019) and Fărăgău (2023). The spectral density expressions for kinetic s_{k}, potential s_{p}, and total s_{total} energies are given by

$$s_{\text{k}}(k_z,t) = \frac{1}{2\pi}\rho\dot{\tilde{u}}(k_z,t)\,\dot{\tilde{u}}^*(k_z,t) = \frac{1}{2\pi}\rho|\dot{\tilde{u}}(k_z,t)|^2, \tag{15}$$

$$s_{\text{p}}(k_z,t) = \frac{1}{\pi}\int_0^t -\text{i}k_z\dot{\tilde{u}}(k_z,\tau)\tilde{\sigma}_{zx}^*(k_z,\tau)\text{d}\tau, \tag{16}$$

$$s_{\text{total}}(k_z,t) = s_{\text{k}}(k_z,t) + s_{\text{p}}(k_z,t), \tag{17}$$

where the tilde represents the quantity in the Fourier-domain, k_z represents the wavenumber, and the asterisk indicates the complex conjugate of the corresponding quantity.

The kinetic $E_{\text{k}}(t)$, potential $E_{\text{p}}(t)$ energy versus time can be obtained by integrating the corresponding spectral quantities over the wavenumber, as follows:

$$E_{\text{k}}(t) = \int_0^{\infty}\text{Re}\Big(s_{\text{k}}(k_z,t)\Big)\text{d}k_z, \qquad E_{\text{p}}(t) = \int_0^{\infty}\text{Re}\Big(s_{\text{p}}(k_z,t)\Big)\text{d}k_z. \tag{18}$$

The total energy $E_{\text{total}}(t)$ is obtained by summing the kinetic and potential energies.

The numerical results of the energy quantities derived in this section are presented in the following sections.

4. Solution method verification and convergence

The solution method described in Section 2.2 introduces two main sources of potential inaccuracies, namely (i) the temporal and spatial discretization, and (ii) the artificial boundaries. These aspects are investigated in this section. The effect of the artificial boundaries is studied in Fig. 3 by comparing the solution $u_{\text{L},1500}$ for a *standard* (used throughout this work) domain $z \in [-1.5,\ 1.5]$ km to the solution $u_{\text{L},6000}$ for a larger domain (i.e., $z \in [-6,\ 6]$ km). It is important to note that the solution is investigated only for time moments before the wave front interacts with the artificial boundary since the solution should approximate the solution of an infinite system. Consequently, the artificial boundaries in the system with larger spatial domain should have a smaller influence on the response compared to the smaller domain. Thus, the solution computed on the larger spatial domain is considered here as benchmark solution. The relative error e is also presented in Fig. 3, and it reads

$$e = \frac{u_{\text{L},1500} - u_{\text{L},6000}}{\max(u_{\text{L},6000})}. \tag{19}$$

Fig. 3 shows that the two displacement fields are indistinguishable and the relative error, which increases with time, reaches a maximum that is 11 orders of magnitude smaller than the response. This is considered sufficiently accurate for the results presented in this work. Consequently, all results in the remainder of the article are computed for $z \in [-1.5,\ 1.5]$ km and $t \in [0,\ 5]$ s.

The convergence of the solution method described in Section 2.2 is presented in Fig. 4 by investigating the behavior of the velocity $\dot{u}$ for different discretizations. The velocity field is chosen to be investigated since the time derivative highlights the small numerical errors and, thus, represents a more strict criterion than the displacement field. The velocity fields are presented at $t = 5$ s (the end of the simulation time) since Fig. 3 showed the largest relative error at $t = 5$ s. The solution clearly converges by decreasing both the temporal and spatial discretization step size. More specifically, decreasing the time step below $\Delta t = 0.5$ ms does not lead to any significant changes, and the same is observed by decreasing the spatial step from $\Delta z = 0.046$ m to $\Delta z = 0.011$ m. Consequently, we can conclude that the solution has converged for $\Delta t = 0.5$ ms and $\Delta z = 0.046$ m.

An additional verification criterion is the energy balance of the equation of motion (Eq. (2)), which is presented in Fig. 5 for decreasing time and spatial steps. An exact solution should lead to a constant total energy E_{total} versus time equal to the initial energy imparted to the system through the initial conditions from Eq. (3). Strictly speaking, only the undamped system should lead to a constant E_{total}, but for

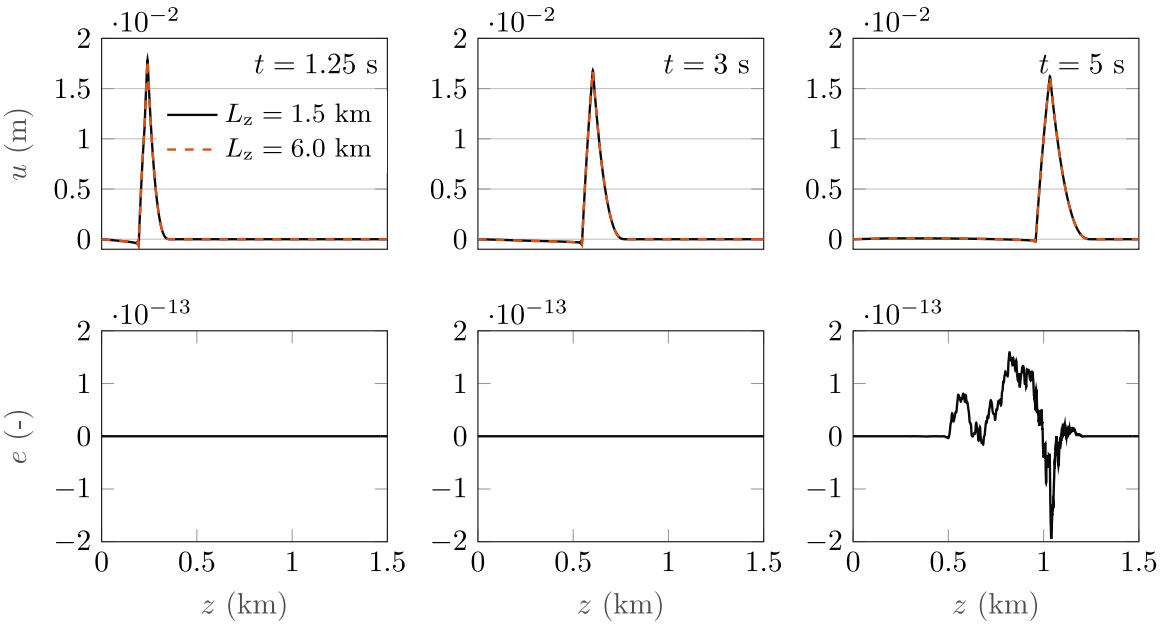

Fig. 3. Response comparison of the systems with domain $z \in [-1.5, 1.5]$ km and $z \in [-6.0, 6.0]$ km for three different time moments (top panels) and the relative error (see Eq. (19)) between the two responses at the same time moments (bottom panels); $\eta = 5 \times 10^{-5}$ s. This figure investigates the effect of the artificial boundaries on the response. (For interpretation of the references to color in this figure legend, the reader is referred to the web version of this article.)

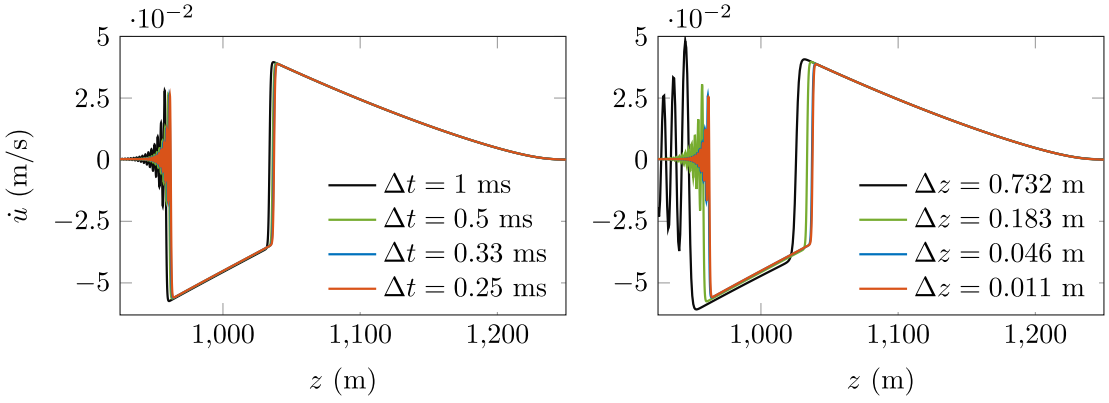

Fig. 4. Response convergence for decreasing the time step (left panel; $\Delta z = 0.046$ m) and for decreasing the spatial step (right panel; $\Delta t = 0.25$ ms). For both panels, the velocity is presented at $t = 5$ s which is the end of the simulation time; $\eta = 5 \times 10^{-5}$ s. (For interpretation of the references to color in this figure legend, the reader is referred to the web version of this article.)

extremely low damping, as is the case here, an almost constant E_{total} is expected. It can be seen that, except for the solution with $\Delta z = 0.73$ m which presents a variation of around 10%, the numerical solution leads to a satisfactory energy balance. When decreasing Δz, the energy converges to a quasi-constant value, as expected for a system with extremely low damping. Surprisingly, decreasing Δt leads to a larger variation E_{total} over time, but the variation for all values of Δt is negligible (less than 1% at its maximum).

To conclude this section, the response obtained using the solution method presented in Section 2.2 with $\Delta z = 0.046$ m and $\Delta t = 0.25$ ms is considered accurate and this spatial and temporal discretization is used for the remainder of the study.

5. The effect of nonlinearity on the response

Different soils exhibit different levels of stiffness reduction for the same level of induced strain. The hyperbolic soil model accounts for this through γ_{ref} and β (see Eq. (1)). The former represents the strain value at which a 50% reduction in shear modulus is observed while the latter controls the variation of degradation with strain level. To investigate the influence of the nonlinearity level on the system response, γ_{ref} is varied. For the same initial conditions, a sufficiently large γ_{ref} leads to a quasi-linear system response, while a small value of γ_{ref} corresponds to a strongly nonlinear system.

Fig. 6 presents the displacement field and corresponding strain-dependent shear modulus for the linear and nonlinear ($\gamma_{\text{ref}} = 0.001$) systems for different time moments to highlight the evolution of the response with time. The initial conditions chosen (see Eq. (3)) imply that the system does not have any initial nonlinearity (zero initial shear strain). Shortly after initiation, a significant amount of nonlinearity develops (the minimum for the chosen $\gamma_{\text{ref}} = 0.001$ is $\frac{G(\gamma)}{G_0} \approx 35\%$). To prohibit the formation of singularities (infinitely large shear strain γ leading to $G(\gamma) = 0$), the dispersion introduced by the higher-order terms generates short wavelength waves in the vicinity of high spatial gradients. This can be seen in the second column of Fig. 6, where $\frac{G(\gamma)}{G_0}$ shows short wavelength fluctuations at the locations of maximum modulus reduction. The dispersion also leads to a reduction over time of the nonlinearity level experienced by the system (i.e., the modulus reduction decreases over time). In other words, initially the nonlinearity is governing the response while after sufficient time, the

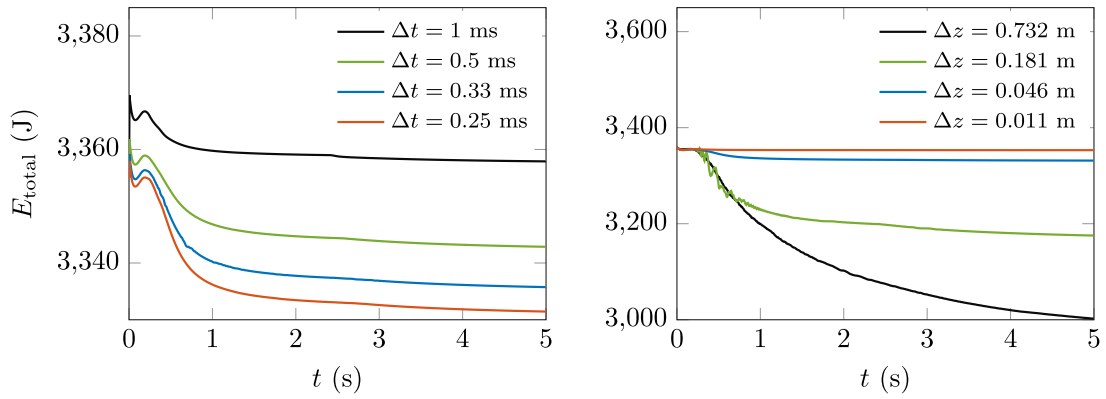

Fig. 5. Convergence of the total energy $E_{\text{total}} = E_{\text{k}} + E_{\text{p}}$ for decreasing the time step (left panel; $\Delta z = 0.046$ m) and for decreasing the spatial step (right panel; $\Delta t = 0.25$ ms); $\eta = 5 \times 10^{-5}$ s. (For interpretation of the references to color in this figure legend, the reader is referred to the web version of this article.)

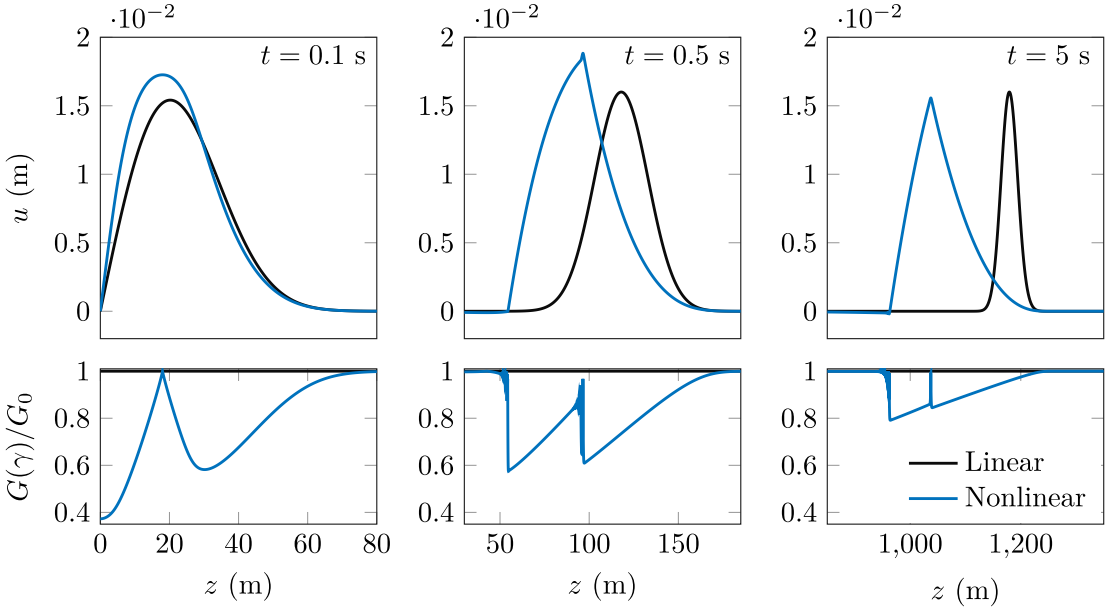

Fig. 6. The displacement fields (top panel) and corresponding shear modulus $G(\gamma(z))$ normalized by the small-strain shear modulus G_0 (bottom panel) for the linear and nonlinear ($\gamma_{\text{ref}} = 0.001$) systems for different time moments; $\eta = 5 \times 10^{-5}$ s. (For interpretation of the references to color in this figure legend, the reader is referred to the web version of this article.)

dispersion causes a reduction in the nonlinearity experienced by the system.

Fig. 7 shows the same quantities as Fig. 6 for different levels of nonlinearity (i.e., varying γ_{ref}). This shows that increasing nonlinearity (decreasing γ_{ref}) leads to a decrease in wave propagation velocity accompanied by a slight increase in wave amplitude, which is intuitive for a softening material. When it comes to the shear modulus reduction, as expected, the shear modulus shows the largest reduction for the smallest γ_{ref}. The largest reduction (i.e., the minimum $\frac{G(\gamma)}{G_0}$) for all levels of nonlinearity is experienced at the *tail* (the wave in Fig. 7 is traveling rightwards) of the main wave (see leftmost vertical dashed line in Fig. 7). The localized point of almost zero modulus reduction (see rightmost vertical dashed line in Fig. 7) is caused by the small strain corresponding to the wave peak. The $\frac{G(\gamma)}{G_0}$ fluctuations observed in the wave tail are caused by the short waves introduced by dispersion. It is known from Dostal et al. (2022) that there is a competition between the two mechanisms (i.e., nonlinearity and dispersion).

For even larger nonlinearity levels, for example if $\frac{G(\gamma)}{G_0} < 10\%$ (obtained if $\gamma_{\text{ref}} < 0.0004$), the numerical scheme described in Section 2.2 does not converge. Nonetheless, the hyperbolic soil model is inaccurate at these large levels of nonlinearity at which plasticity most likely develops. The nonlinear gradient model presented in this study is suitable from small to medium–large strain levels, but unsuitable for extremely large ones.

6. The effect of nonlinearity on the system energy

To investigate the effect of nonlinearity on the system energy, we analyze the evolution of the kinetic and potential energy of the system with time. Fig. 8 presents the aforementioned quantities for different levels of nonlinearity. Note that for ease of results interpretation, the damping term is set to zero in Fig. 8. The total energy, not presented here for brevity, for all nonlinearity levels is quasi-constant since the considered system is conservative (no damping); the strongly nonlinear scenarios present a very small variation of the total energy with time due to small numerical errors (see Section 4), but this is negligible.

The linear system shows that after an initial exchange between kinetic and potential energy, they become constant for the rest of time. Unlike the linear system, the nonlinear scenarios show a continuous exchange between kinetic and potential energy. More specifically, the kinetic energy decreases while the potential one increases, confirming the observation that the bulk of the wave slows down with increasing

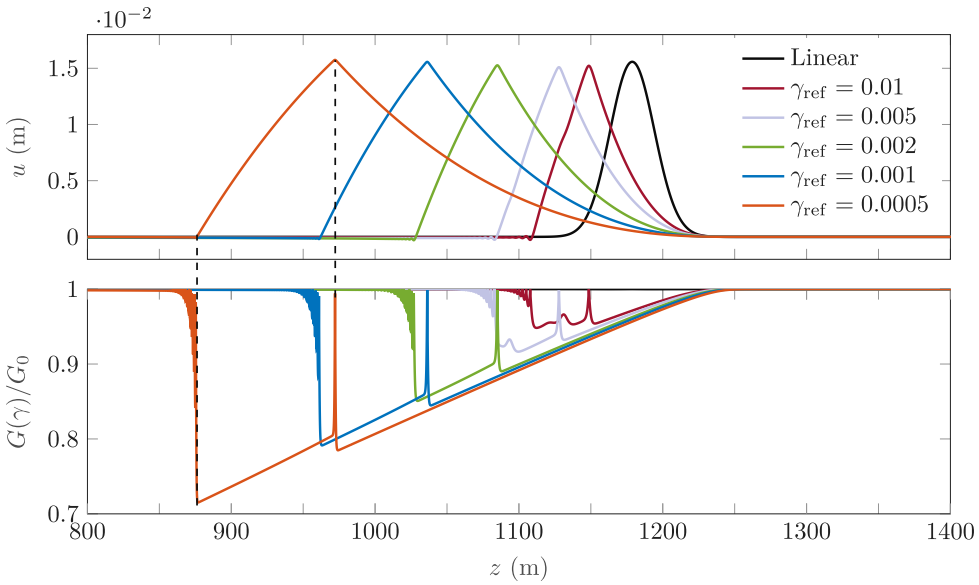

Fig. 7. The displacement fields (top panel) and corresponding shear modulus $G(\gamma(z))$ normalized by the small-strain shear modulus G_0 (bottom panel) for different levels of nonlinearity by varying γ_{ref}. The results are presented at $t = 5\,\text{s}$; $\eta = 5 \times 10^{-5}$ s. (For interpretation of the references to color in this figure legend, the reader is referred to the web version of this article.)

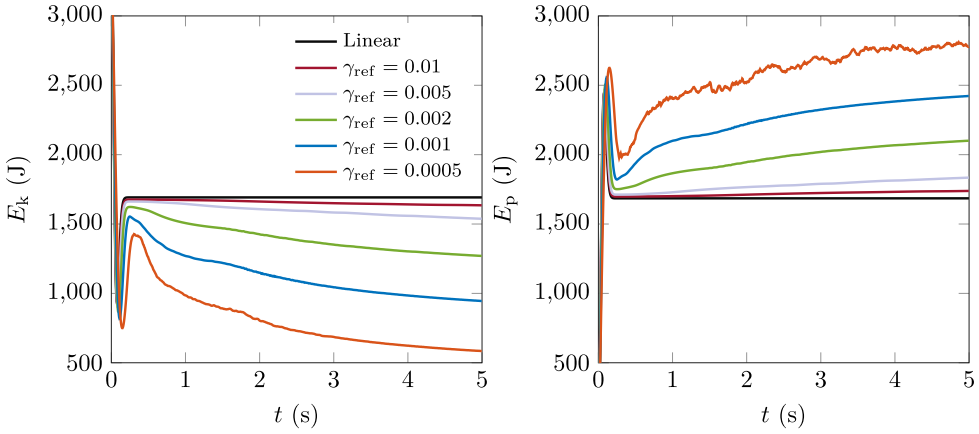

Fig. 8. The temporal evolution of the kinetic (left panel) and potential (right panel) energy for different level of nonlinearity. For ease and clarity of results interpretation, damping has been neglected in these results (i.e., $\eta = 0$ s). (For interpretation of the references to color in this figure legend, the reader is referred to the web version of this article.)

nonlinearity level. Nonetheless, the exchange between the two seems to decrease with time, indicating that a constant value can be reached at sufficiently large time moments.

Fig. 9 presents the spectral total energy density versus time and wavenumber for the linear and nonlinear (undamped and damped) systems. On the one hand, the linear system shows that the energy remains constant versus time for all wavenumbers. It is well known that energy cannot be transferred among wavenumbers (or frequencies) in linear systems, and this is correctly demonstrated by the results of the linear system. On the other hand, the nonlinear system can and does exhibit energy transfer between wavenumbers with time; it can be seen clearly in the nonlinear undamped scenario (middle panel of Fig. 9) that some content is transferred to higher wavenumbers for increasing time, forming large peaks at high wavenumbers. However, these peaks disappear almost completely in the lightly damped system, suggesting that they are not of physical relevance.

To further investigate the high-wavenumber peaks, Fig. 10 presents the total spectral energy density at $t = 3\,\text{s}$ for varying levels of nonlinearity in the undamped system. The large peaks appear in the spectral energy at all levels of nonlinearity. However, these peaks do not contain significant amount of energy, as the cumulative integral shows in the bottom panel of Fig. 10. This fact together with their disappearing almost completely in the presence of damping implies that they are not of physical relevance.

7. The formation of small-amplitude waves traveling in the direction opposite to the main wave

In all results computed one interesting feature is persistent. Although the system is homogeneous, some time after initiation, a small-amplitude wave is generated that propagates in the direction opposite to the main pulse. Fig. 11 presents snapshots of the stress profile at different time moments to highlight the emergence of the backward propagating wave. Note that, unlike previous sections, also the negative spatial axis is presented here to emphasize that the generated wave propagates in direction opposite to the main wave. It can be seen that prior to $t = 2\,\text{s}$ the whole response is propagating outwards. At $t = 3\,\text{s}$ two wave-fronts are observed that propagate inward (see panels at $t = 3.5\,\text{s}$ and $t = 4.5\,\text{s}$) at the linear-wave speed due to the associated small strains. The two wave fronts intersect at $z = 0\,\text{m}$ and continue their propagation.

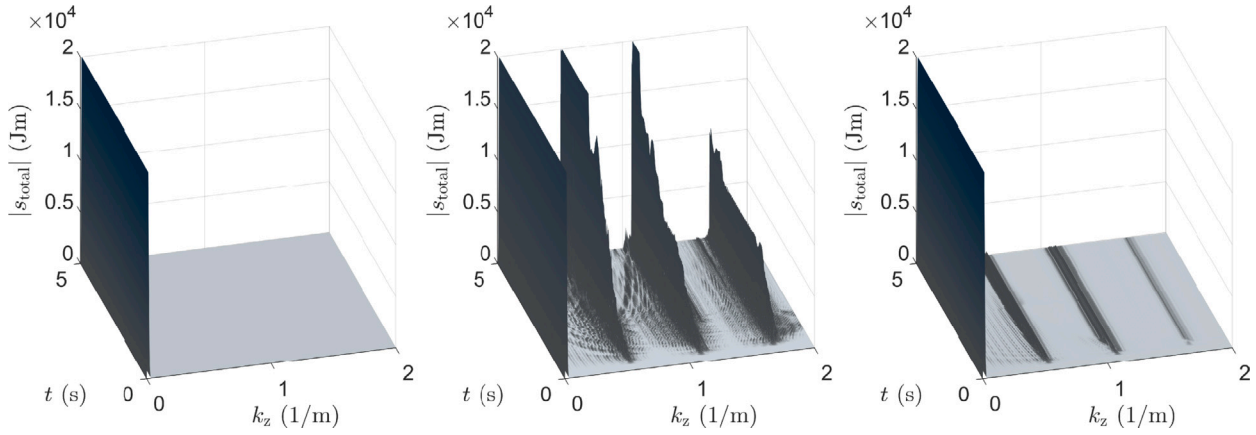

Fig. 9. The total spectral energy density versus time and wavenumber k_z for the linear (left panel), nonlinear undamped (middle panel; $\gamma_{\text{ref}} = 0.001$, $\eta = 0$ s), and nonlinear damped (right panel; $\gamma_{\text{ref}} = 0.001$, $\eta = 5 \times 10^{-5}$ s) scenarios.

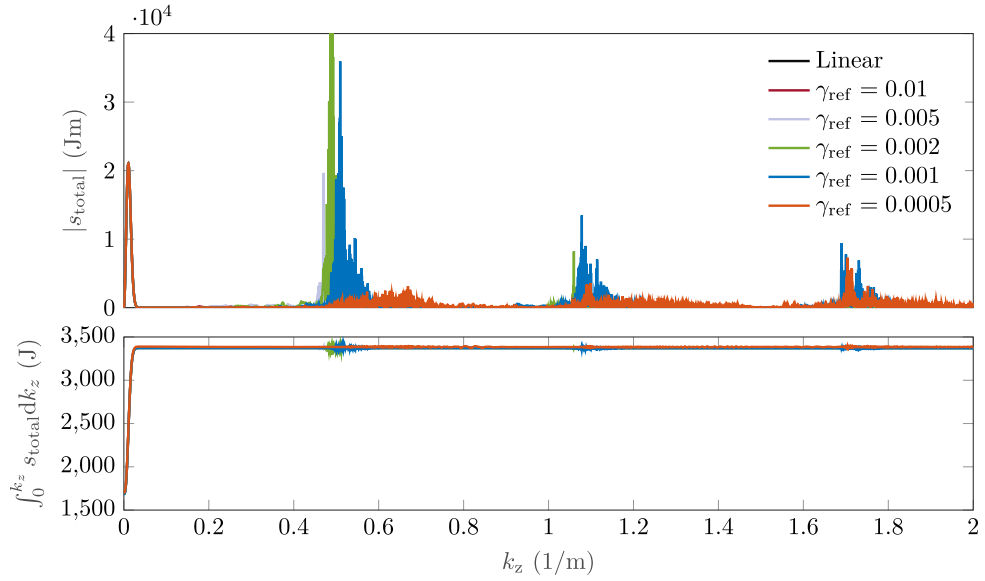

Fig. 10. The total spectral energy density (top panel) and the cumulative energy versus wavenumber (bottom panel) of the nonlinear and undamped system at $t = 3$ s for varying nonlinearity levels; $\eta = 0$ s. (For interpretation of the references to color in this figure legend, the reader is referred to the web version of this article.)

To demonstrate the energy is indeed propagating in direction opposite to the main waves, Fig. 12 presents the power flux $P_{\text{f}} = \sigma_{zx}\dot{u}$ at cross-section $x = 200$ m. Looking at the left panel, it appears that all energy is crossing this section in positive x-direction (i.e., positive power flux P_{f}), as one would expect. Nonetheless, a very small amount of energy is propagating in negative z-direction as indicated by the sharp drop observed at $t \approx 4$ s leading to a negative power flux thereafter. This sharp drop occurs when the wave front of the backward propagating wave crosses the section $x = 200$ m confirming that it carries energy in the direction opposite to the main wave.

To eliminate the possibility of this being a numerical artifact, Fig. 13 shows the convergence study presented in Section 4 with a focus on the backward propagating wave. Fig. 13 shows that this feature is not a numerical artifact and that the solution previously investigated is converged.

To explain the mechanisms causing this feature, the response evolution discussed in previous section is repeated here. The system does initially not present any nonlinearity due to the initial conditions chosen. The nonlinearity evolves with time leading to a sharpening peak that eventually would cause a singularity in the strain/stress response. The singularity is not allowed to develop due to the dispersion introduced by the higher-order terms. Consequently, the dispersion is only significantly activated right before the singularity develops. The backward-propagating wave appears to be a product of this interaction of nonlinearity with dispersion. To demonstrate this, Fig. 14 presents the backward propagating waves for different levels of nonlinearity. The singularity would, in the absence of dispersion, develop quicker in the highly nonlinear system ($\gamma_{\text{red}} = 0.001$) while it would take longer for a more moderate nonlinearity level ($\gamma_{\text{red}} = 0.002$). This leads to the backward propagating wave to emerge later in the moderately nonlinear system compared to the highly nonlinear one, which is confirmed in Fig. 14. Moreover, it can be seen that the higher the nonlinearity, the more pronounced this feature, albeit a very small feature in both cases.

It must be emphasized that the small amplitude associated to the backward propagating wave could diminish its practical relevance. Nonetheless, its small amplitude observed for this type of initial conditions does not eliminate the possibility of this feature being more pronounced in other scenarios. Moreover, the emergence of a wave carrying energy in opposite direction is not intuitive in a homogeneous system. It is known that nonlinearity can transfer energy over wavenumbers, but the fact that it transfers energy (albeit a very low amount) to negative wavenumbers comes as a surprise, at least to the authors.

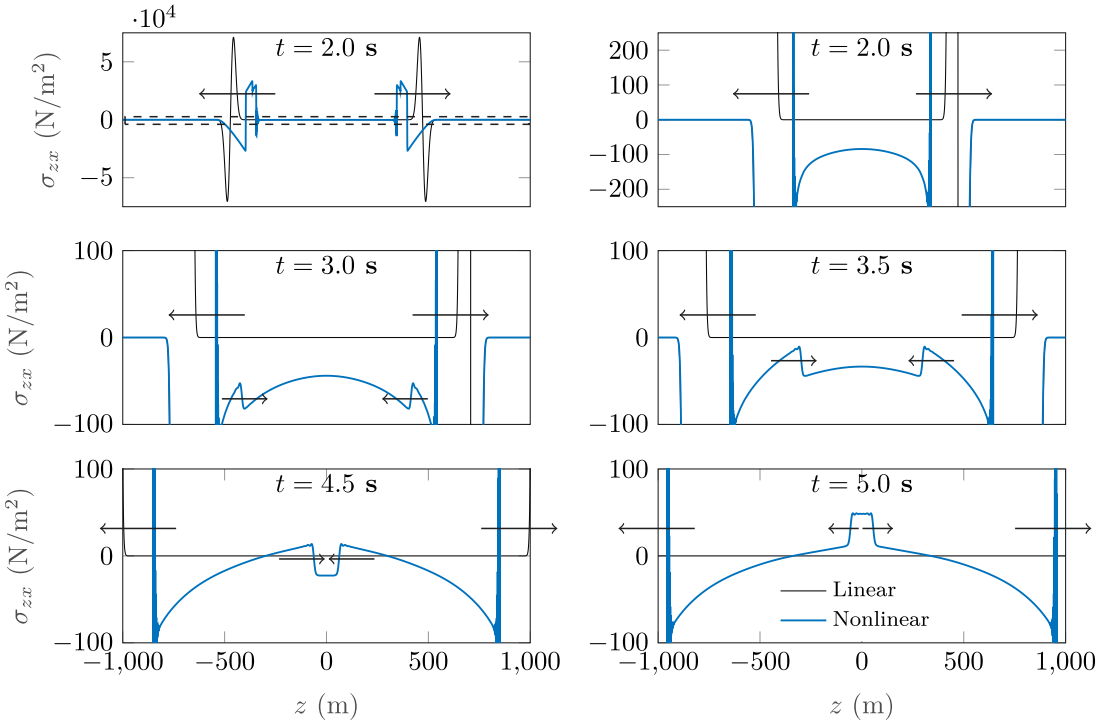

Fig. 11. The spatial profile of the shear stress σ_{zx} of the linear (black lines) and nonlinear (blue lines; $\gamma_{\text{ref}} = 0.001$) systems for different time moments. The top right panel is a zoom-in of top left panel as indicated by the dashed-line rectangle. The arrows indicate the propagation direction of the waves; $\eta = 5 \times 10^{-5}$ s. (For interpretation of the references to color in this figure legend, the reader is referred to the web version of this article.)

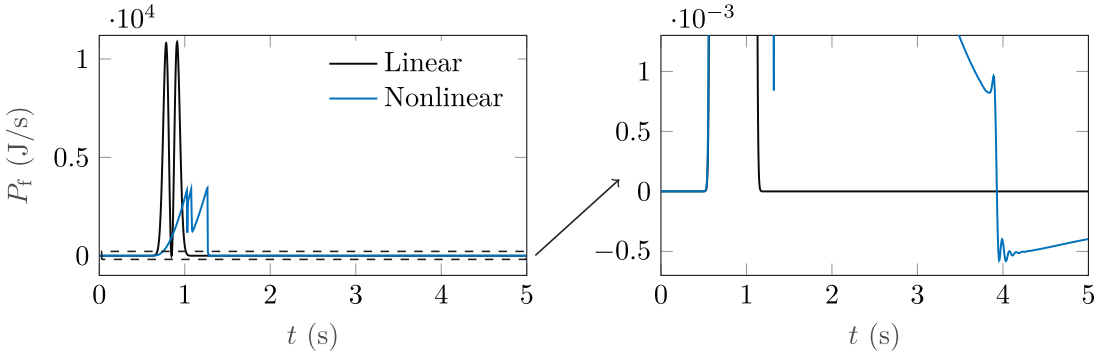

Fig. 12. The power flux P_{f} through a cross-section at $x = 200$ m for the linear and nonlinear ($\gamma_{\text{ref}} = 0.001$) systems. The right panel is a zoom-in of the left one to focus on the power flux associated to the backward propagating wave; $\eta = 5 \times 10^{-5}$ s. (For interpretation of the references to color in this figure legend, the reader is referred to the web version of this article.)

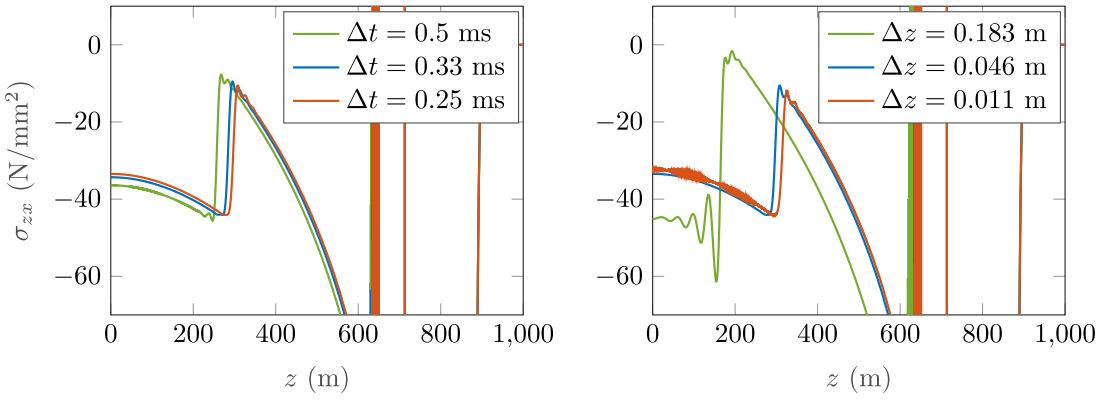

Fig. 13. Response convergence for decreasing the time step (left panel; $\Delta z = 0.046$ m) and for decreasing the spatial step (right panel; $\Delta t = 0.25$ ms) with focus on the backward propagating waves; $\eta = 5 \times 10^{-5}$ s, $t = 3.5$ s. (For interpretation of the references to color in this figure legend, the reader is referred to the web version of this article.)

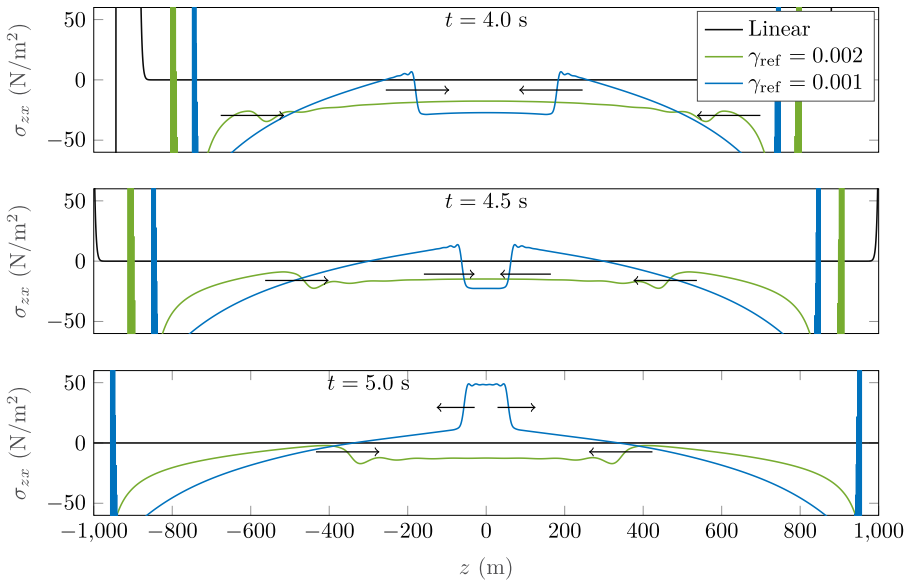

Fig. 14. The spatial profile of the shear stress σ_{zx} for different levels of nonlinearity (i.e., varying γ_{ref}) at different time moments focusing on the small-amplitude backward propagating wave. The arrows indicate the propagation direction of the waves; $\eta = 5 \times 10^{-5}$ s. (For interpretation of the references to color in this figure legend, the reader is referred to the web version of this article.)

8. Conclusions

The authors previously presented a novel nonlinear 1-D gradient model that integrates (i) higher-order gradient terms to account for small-scale material heterogeneity, and (ii) a hyperbolic model to describe nonlinear softening material behavior. While the earlier work primarily investigated the existence and properties of *solitary*-type waves, the current study focused on the *transient* wave propagation in the aforementioned nonlinear gradient model.

The findings suggest that with increasing nonlinearity, the main wave decelerates and its shape becomes significantly distorted compared to the linear system's response. This demonstrates that using a linear material model for predicting the seismic site response at moderate to large strains can lead to significant errors. The energy analysis shows that, unlike the linear system, the nonlinear system exhibits a continuous energy exchange where the kinetic energy decreases while the potential energy increases over time. Additionally, the wavenumber spectrum of the nonlinear-elastic response shows peaks at high wavenumbers. However, these peaks are eliminated with the introduction of a small amount of linear viscous damping, indicating their lack of physical relevance.

A notable feature that persists despite the presence of damping is the formation of small-amplitude waves traveling in the direction opposite to the main wave. Generalized continua, such as gradient elasticity models, can only predict heterogeneity effects at much larger spatial scales, missing the small energy scatter from minor heterogeneity traveling opposite to the main wave. This study demonstrates that incorporating material nonlinearity into such a homogeneous generalized continuum can capture this reverse energy propagation, albeit at magnitudes much smaller than the main wave. To the best of the authors' knowledge, this phenomenon has not been previously reported.

These insights highlight the characteristics of the proposed nonlinear 1-D gradient model and its potential applicability in scenarios such as predicting seismic site responses.

CRediT authorship contribution statement

Andrei B. Fărăgău: Writing – original draft, Visualization, Software, Methodology, Investigation, Formal analysis, Conceptualization. **Marten Hollm:** Writing – review & editing, Software, Methodology, Investigation, Conceptualization. **Leo Dostal:** Writing – review & editing, Supervision, Methodology, Investigation, Conceptualization. **Andrei V. Metrikine:** Writing – review & editing, Supervision, Investigation, Conceptualization. **Karel N. van Dalen:** Writing – review & editing, Supervision, Methodology, Investigation, Formal analysis, Conceptualization.

Declaration of competing interest

The authors declare that they have no known competing financial interests or personal relationships that could have appeared to influence the work reported in this paper.

Appendix. Remarks about the numerical scheme

The space derivatives appearing in Eq. (10) are discretized. In order to simplify the notation, the time index n is omitted in the following, such that $\mathbf{u}^n$ and u_i^n are written as $\mathbf{u}$ and u_i, respectively. Using standard finite-difference approximations in space, which have an accuracy of $\mathcal{O}(\Delta z^2)$, it holds

$$u_{i,z} = \frac{u_{i+1} - u_{i-1}}{2\Delta z} + \mathcal{O}(\Delta z^2), \tag{A.1}$$

$$u_{i,zz} = \frac{u_{i+1} - 2u_i + u_{i-1}}{\Delta z^2} + \mathcal{O}(\Delta z^2), \tag{A.2}$$

$$\begin{aligned} h_{,z}(u_{i,z}) =& \frac{h(u_{i+1,z}) - h(u_{i-1,z})}{2\Delta z} + \mathcal{O}(\Delta z^2) \\ =& \frac{1}{2\Delta z} \left\{ \frac{G_0}{1 + \left(\frac{\sqrt{3}}{2} \frac{|u_{i+2} - u_i|}{2\Delta z \gamma_{\text{ref}}} \right)^{\beta}} \frac{u_{i+2} - u_i}{2\Delta z} \right. \\ & \left. - \frac{G_0}{1 + \left(\frac{\sqrt{3}}{2} \frac{|u_i - u_{i-2}|}{2\Delta z \gamma_{\text{ref}}} \right)^{\beta}} \frac{u_i - u_{i-2}}{2\Delta z} \right\} + \mathcal{O}(\Delta z^2), \end{aligned} \tag{A.3}$$

$$
\begin{aligned}
h_{,zzz}(u_{i,z}) &= \frac{h(u_{i+2,z}) - 2h(u_{i+1,z}) + 2h(u_{i-1,z}) - h(u_{i-2,z})}{2\Delta z^3} + \mathcal{O}(\Delta z^2) \\
&= \frac{1}{2\Delta z^3} \left\{ \frac{G_0}{1 + \left(\frac{\sqrt{3}}{2} \frac{|u_{i+3} - u_{i+1}|}{2\Delta z \gamma_{\text{ref}}} \right)^{\beta}} \frac{u_{i+3} - u_{i+1}}{2\Delta z} \right. \\
&\quad - 2 \frac{G_0}{1 + \left(\frac{\sqrt{3}}{2} \frac{|u_{i+2} - u_i|}{2\Delta z \gamma_{\text{ref}}} \right)^{\beta}} \frac{u_{i+2} - u_i}{2\Delta z} \\
&\quad + 2 \frac{G_0}{1 + \left(\frac{\sqrt{3}}{2} \frac{|u_i - u_{i-2}|}{2\Delta z \gamma_{\text{ref}}} \right)^{\beta}} \frac{u_i - u_{i-2}}{2\Delta z} \\
&\quad \left. - \frac{G_0}{1 + \left(\frac{\sqrt{3}}{2} \frac{|u_{i-1} - u_{i-3}|}{2\Delta z \gamma_{\text{ref}}} \right)^{\beta}} \frac{u_{i-1} - u_{i-3}}{2\Delta z} \right\} + \mathcal{O}(\Delta z^2).
\end{aligned} \tag{A.4}
$$

Since Eq. (8) is nonlinear, a numerical scheme has to be used to calculate u_i^{n+1} iteratively. For this, Newton's method is used, for which the computation of the Jacobian matrix is necessary. Using $|x|_{,x} = \operatorname{sgn}(x)$, $\operatorname{sgn}(x)x = |x|$, and defining

$$
q(x, y) := \frac{1 + (1 - \beta) \left(\frac{\sqrt{3}}{2} \frac{|x - y|}{2\Delta z \gamma_{\text{ref}}} \right)^{\beta}}{16\Delta z^4 \left(1 + \left(\frac{\sqrt{3}}{2} \frac{|x - y|}{2\Delta z \gamma_{\text{ref}}} \right)^{\beta} \right)^2}, \tag{A.5}
$$

it follows that the entries of the Jacobian are given by

$$
\begin{aligned}
\frac{\partial f_i}{\partial u_{i+3}}(\mathbf{u}) &= B_1 L^2 G_0 \, q(u_{i+3}, u_{i+1}), \\
\frac{\partial f_i}{\partial u_{i-3}}(\mathbf{u}) &= B_1 L^2 G_0 \, q(u_{i-1}, u_{i-3}), \\
\frac{\partial f_i}{\partial u_{i+2}}(\mathbf{u}) &= -G_0 \left(\Delta z^2 + 4B_2 \frac{\rho L^2 \Delta z^2}{G_0 \Delta t^2} + 2B_1 L^2 \right) q(u_{i+2}, u_i), \\
\frac{\partial f_i}{\partial u_{i-2}}(\mathbf{u}) &= -G_0 \left(\Delta z^2 + 4B_2 \frac{\rho L^2 \Delta z^2}{G_0 \Delta t^2} + 2B_1 L^2 \right) q(u_i, u_{i-2}), \\
\frac{\partial f_i}{\partial u_i}(\mathbf{u}) &= \frac{\rho}{\Delta t^2} + \frac{G_0 \eta}{\Delta t \Delta z^2} - \frac{\partial f_i}{\partial u_{i+2}}(\mathbf{u}) - \frac{\partial f_i}{\partial u_{i-2}}(\mathbf{u}), \\
\frac{\partial f_i}{\partial u_{i+1}}(\mathbf{u}) &= -\frac{G_0 \eta}{2\Delta t \Delta z^2} - \frac{\partial f_i}{\partial u_{i+3}}(\mathbf{u}), \\
\frac{\partial f_i}{\partial u_{i-1}}(\mathbf{u}) &= -\frac{G_0 \eta}{2\Delta t \Delta z^2} - \frac{\partial f_i}{\partial u_{i-3}}(\mathbf{u}), \\
\frac{\partial f_i}{\partial u_j}(\mathbf{u}) &= 0, \qquad \text{for } |i - j| > 3.
\end{aligned} \tag{A.6}
$$

Data availability

No data was used for the research described in the article.

References

Abali, B.E., Müller, W.H., Dell'Isola, F., 2017. Theory and computation of higher gradient elasticity theories based on action principles. Arch. Appl. Mech. 87 (9), 1495–1510. http://dx.doi.org/10.1007/s00419-017-1266-5.

Aifantis, E.C., 1987. The physics of plastic deformation. Int. J. Plast. 3 (3), 211–247. http://dx.doi.org/10.1016/0749-6419(87)90021-0.

Altan, B.S., Aifantis, E.C., 1997. On some aspects in the special theory of gradient elasticity. J. Mech. Behav. Mater. 8 (3).

Andrianov, I.V., Awrejcewicz, J., Danishevs'Kyy, V.V., Weichert, D., 2011. Wave propagation in periodic composites: Higher-order asymptotic analysis versus plane-wave expansions method. J. Comput. Nonlinear Dyn. 6 (1), 1–8. http://dx.doi.org/10.1115/1.4002389.

Andrianov, I.V., Bolshakov, V.I., Danishevs'kyy, V.V., Weichert, D., 2008. Higher order asymptotic homogenization and wave propagation in periodic composite materials. Proc. R. Soc. Lond. Ser. A Math. Phys. Eng. Sci. 464 (2093), 1181–1201. http://dx.doi.org/10.1098/rspa.2007.0267.

Anicode, S.V.K., Zhang, Y., Mitts, C., Aifantis, E., Madenci, E., 2024. Peridynamic correspondence model with strain gradient elasticity for microstructure dependent size effects. Comput. Methods Appl. Mech. Engrg. 425, 116927. http://dx.doi.org/10.1016/j.cma.2024.116927.

Askes, H., Aifantis, E.C., 2011. Gradient elasticity in statics and dynamics: An overview of formulations, length scale identification procedures, finite element implementations and new results. Int. J. Solids Struct. 48 (13), 1962–1990. http://dx.doi.org/10.1016/j.ijsolstr.2011.03.006.

Askes, H., Metrikine, A.V., Pichugin, A.V., Bennett, T., 2008. Four simplified gradient elasticity models for the simulation of dispersive wave propagation. Phil. Mag. 88 (28–29), 3415–3443. http://dx.doi.org/10.1080/14786430802524108.

Behnam-Rasouli, M.S., Challamel, N., Karamodin, A., Sani, A.A., 2024. Application of the green's function method for static analysis of nonlocal stress-driven and strain gradient elastic nanobeams. Int. J. Solids Struct. 295, http://dx.doi.org/10.1016/j.ijsolstr.2024.112794.

Capdeville, Y., Guillot, L., Marigo, J.J., 2010. 1-d non-periodic homogenization for the seismic wave equation. Geophys. J. Int. 181 (2), 897–910. http://dx.doi.org/10.1111/j.1365-246X.2010.04529.x.

Castelluccio, G.M., Lim, H., Emery, J.M., Battaile, C.C., 2021. Crack tip microplasticity mediated by microstructure gradients. Fatigue Fract. Eng. Mater. Struct. 44 (9), 2337–2355. http://dx.doi.org/10.1111/ffe.13493.

Chang, C.S., Gao, J., 1995. Second-gradient constitutive theory for granular material with random packing structure. Int. J. Solids Struct. 32 (16), 2279–2293. http://dx.doi.org/10.1016/0020-7683(94)00259-Y.

Craster, R.V., Kaplunov, J., Pichugin, A.V., 2010. High-frequency homogenization for periodic media. Proc. R. Soc. Lond. Ser. A Math. Phys. Eng. Sci. 466 (2120), 2341–2362. http://dx.doi.org/10.1098/rspa.2009.0612.

de Oliveira Barbosa, J.M., Fărăgău, A.B., van Dalen, K.N., 2021. A lattice model for transition zones in ballasted railway tracks. J. Sound Vib. 494, 115840. http://dx.doi.org/10.1016/j.jsv.2020.115840.

de Oliveira Barbosa, J.M., Fărăgău, A.B., van Dalen, K.N., Steenbergen, M., 2022. Modelling ballast via a non-linear lattice to assess its compaction behaviour at railway transition zones. J. Sound Vib. 530, 116942. http://dx.doi.org/10.1016/j.jsv.2022.116942.

Dell'Isola, F., Steigmann, D., 2015. A two-dimensional gradient-elasticity theory for woven fabrics. J. Elasticity 118 (1), 113–125. http://dx.doi.org/10.1007/s10659-014-9478-1.

Dell'isola, F., Steigmann, D.J., 2020. Discrete and continuum models for complex metamaterials. In: Discrete and Continuum Models for Complex Metamaterials. pp. 1–398. http://dx.doi.org/10.1017/9781316104262.

Dostal, L., Hollm, M., Metrikine, A.V., Tsouvalas, A., van Dalen, K.N., 2022. Localized stationary seismic waves predicted using a nonlinear gradient elasticity model. Nonlinear Dynam. 107 (1), 1107–1125. http://dx.doi.org/10.1007/s11071-021-06981-4, arXiv:2011.12852.

Fărăgău, A.B., 2023. Understanding Degradation Mechanisms at Railway Transition Zones Using Phenomenological Models (Ph.D. thesis). Delft University of Technology.

Fărăgău, A.B., de Oliveira Barbosa, J.M., Metrikine, A.V., van Dalen, K.N., 2022. Dynamic amplification in a periodic structure with a transition zone subject to a moving load: three different phenomena. Math. Mech. Solids 27 (9), 1740–1760. http://dx.doi.org/10.1177/10812865221094318.

Fărăgău, A.B., Metrikine, A.V., van Dalen, K.N., 2019. Transition radiation in a piecewise-linear and infinite one-dimensional structure–a Laplace transform method. Nonlinear Dynam. 98, 2435–2461. http://dx.doi.org/10.1007/s11071-019-05083-6.

Fish, J., Chen, W., Nagai, G., 2002. Non-local dispersive model for wave propagation in heterogeneous media: Multi-dimensional case. Internat. J. Numer. Methods Engrg. 54 (3), 347–363. http://dx.doi.org/10.1002/nme.424.

Geers, M.G., Kouznetsova, V., Brekelmans, W.A., 2001. Gradient-enhanced computational homogenization for the micro-macro scale transition. J. Phys. IV : JP 11 (5), http://dx.doi.org/10.1051/jp4:2001518.

Georgiadis, H.G., Vardoulakis, I., Lykotrafitis, G., 2000. Torsional surface waves in a gradient-elastic half-space. Wave Motion 31 (4), 333–348. http://dx.doi.org/10.1016/S0165-2125(99)00035-9.

Gholami, Y., Ansari, R., Gholami, R., 2020. Three-dimensional nonlinear primary resonance of functionally graded rectangular small-scale plates based on strain gradeint elasticity theory. Thin-Walled Struct. 150, 106681. http://dx.doi.org/10.1016/j.tws.2020.106681.

Gómez-Silva, F., Askes, H., 2024. Variationally consistent elishakoff beam theory: Two finite element implementations and application to flexural wave propagation in carbon nanotubes. J. Sound Vib. 580, 118388. http://dx.doi.org/10.1016/j.jsv.2024.118388.

Gómez-Silva, F., Zaera, R., 2023. Low-order continualization of an anisotropic membrane lattice with next-nearest interactions. Enhanced prediction of its dynamic behaviour. Eur. J. Mech. A Solids 97, 104801. http://dx.doi.org/10.1016/j.euromechsol.2022.104801.

Gourgiotis, P.A., Georgiadis, H.G., 2009. Plane-strain crack problems in microstructured solids governed by dipolar gradient elasticity. J. Mech. Phys. Solids 57 (11), 1898–1920. http://dx.doi.org/10.1016/j.jmps.2009.07.005.

Gusev, A.A., Lurie, S.A., 2017. Symmetry conditions in strain gradient elasticity. Math. Mech. Solids 22 (4), 683–691. http://dx.doi.org/10.1177/1081286515606960.

Hardin, B.O., Drnevich, V.P., 1972. Shear modulus and damping in soils: Measurement and parameter effects. J. Soil Mech. Found. Div. 98 (6), 603–624. http://dx.doi.org/10.1061/jsfeaq.0001756.

Huang, Y., Zhang, L., Guo, T.F., Hwang, K.C., 1997. Mixed mode near-tip fields for cracks in materials with strain-gradient effects. J. Mech. Phys. Solids 45 (3), 439–465. http://dx.doi.org/10.1016/S0022-5096(96)00089-0.

Kouznetsova, V., Geers, M.G., Brekelmans, W.A., 2002. Multi-scale constitutive modelling of heterogeneous materials with a gradient-enhanced computational homogenization scheme. Internat. J. Numer. Methods Engrg. 54, 1235–1260.

Kramer, S.L., 1996. In: Hal, W.J. (Ed.), Geotechnical Earthquake Engineering. Prentice Hall, Upper Saddle River.

Lasry, D., Belytschko, T., 1988. Localization limiters in transient problems. Int. J. Solids Struct. 24 (6), 581–597. http://dx.doi.org/10.1016/0020-7683(88)90059-5.

Liebold, C., Müller, W.H., 2016. Comparison of gradient elasticity models for the bending of micromaterials. Comput. Mater. Sci. 116, 52–61. http://dx.doi.org/10.1016/j.commatsci.2015.10.031.

Lurie, S.A., Kalamkarov, A.L., Solyaev, Y.O., Volkov, A.V., 2021. Dilatation gradient elasticity theory. Eur. J. Mech. A Solids 88, 104258. http://dx.doi.org/10.1016/j.euromechsol.2021.104258.

Ma, X., Sahmani, S., Safaei, B., 2022. Quasi-3D large deflection nonlinear analysis of isogeometric fgm microplates with variable thickness via nonlocal stress–strain gradient elasticity. Eng. Comput. 38 (4), 3691–3704. http://dx.doi.org/10.1007/s00366-021-01390-y.

Metrikine, A.V., 2006. On causality of the gradient elasticity models. J. Sound Vib. 297 (3–5), 727–742. http://dx.doi.org/10.1016/j.jsv.2006.04.017.

Metrikine, A.V., Askes, H., 2002. One-dimensional dynamically consistent gradient elasticity models derived from a discrete microstructure: Part 1: Generic formulation. Eur. J. Mech. A Solids 21 (4), 555–572. http://dx.doi.org/10.1016/S0997-7538(02)01218-4.

Mindlin, R.D., 1964. Micro-structure in linear elasticity. Arch. Ration. Mech. Anal. 16 (1), 51–78. http://dx.doi.org/10.1007/BF00248490.

Mühlhaus, H.B., Oka, F., 1996. Dispersion and wave propagation in discrete and continuous models for granular materials. Int. J. Solids Struct. 33 (19), 2841–2858. http://dx.doi.org/10.1016/0020-7683(95)00178-6.

Nguyen, B.H., Zhuang, X., Rabczuk, T., 2019. NURBS-based formulation for nonlinear electro-gradient elasticity in semiconductors. Comput. Methods Appl. Mech. Engrg. 346, 1074–1095. http://dx.doi.org/10.1016/j.cma.2018.08.026.

Papargyri-Beskou, S., Tsinopoulos, S.V., Beskos, D.E., 2011. Transient dynamic analysis of a fluid-saturated porous gradient elastic column. Acta Mech. 222 (3–4), 351–362. http://dx.doi.org/10.1007/s00707-011-0539-2.

Patnaik, S., Sidhardh, S., Semperlotti, F., 2021. Towards a unified approach to nonlocal elasticity via fractional-order mechanics. Int. J. Mech. Sci. 189, 105992. http://dx.doi.org/10.1016/j.ijmecsci.2020.105992.

Peerlings, R.H.J., de Borst, R., Brekelmans, W.A.M., de Vree, J.H.P., 1996. Gradient enhanced damage for quasi-brittle materials. Internat. J. Numer. Methods Engrg. 39, 3391–3403.

Pirmoradi, P., Suiker, A.S., Poorsolhjouy, P., 2024. Anisotropic elastic strain-gradient continuum from the macro-scale to the granular micro-scale. J. Elasticity http://dx.doi.org/10.1007/s10659-024-10063-y.

Podulka, P., Macek, W., 2024. Saint-venant torsion based on strain gradient theory. Int. J. Mech. Sci. 269, http://dx.doi.org/10.1016/j.ijmecsci.2024.109069.

Polizzotto, C., 2017. A hierarchy of simplified constitutive models within isotropic strain gradient elasticity. Eur. J. Mech. A Solids 61, 92–109. http://dx.doi.org/10.1016/j.euromechsol.2016.09.006.

Rubin, M.B., Rosenau, P., Gottlieb, O., 1995. Continuum model of dispersion caused by an inherent material characteristic length. J. Appl. Phys. 77 (8), 4054–4063. http://dx.doi.org/10.1063/1.359488.

Schreyer, H.L., Chen, Z., 1986. One-dimensional softening with localization. J. Appl. Mech. Trans. ASME 53 (4), 791–797. http://dx.doi.org/10.1115/1.3171860.

Sluys, L.J., de Borst, R., 1992. Wave propagation and localization in a rate-dependent cracked medium-model formulation and one-dimensional examples. Int. J. Solids Struct. 29 (23), 2945–2958. http://dx.doi.org/10.1016/0020-7683(92)90151-I.

Suiker, A.S., De Borst, R., Chang, C.S., 2001. Micro-mechanical modelling of granular material. Part 1: Derivation of a second-gradient micro-polar constitutive theory. Acta Mech. 149 (1–4), 161–180. http://dx.doi.org/10.1007/BF01261670.

Tarasov, V.E., Aifantis, E.C., 2015. Non-standard extensions of gradient elasticity: Fractional non-locality, memory and fractality. Commun. Nonlinear Sci. Numer. Simul. 22 (1–3), 197–227. http://dx.doi.org/10.1016/j.cnsns.2014.10.002.

Torabi, J., Niiranen, J., Ansari, R., 2021. Nonlinear finite element analysis within strain gradient elasticity: Reissner-Mindlin plate theory versus three-dimensional theory. Eur. J. Mech. A Solids 87, 104221. http://dx.doi.org/10.1016/j.euromechsol.2021.104221.

Tran, L.V., Niiranen, J., 2020. A geometrically nonlinear Euler–Bernoulli beam model within strain gradient elasticity with isogeometric analysis and lattice structure applications. Math. Mech. Complex Syst. 8 (4).

Triantafyllidis, N., Aifantis, E.C., 1986. A gradient approach to localization of deformation. I. Hyperelastic materials. J. Elasticity 16, 225–237. http://dx.doi.org/10.1137/1.9781611972795.88.

van Dalen, K.N., Tsouvalas, A., Metrikine, A.V., Hoving, J.S., 2015. Transition radiation excited by a surface load that moves over the interface of two elastic layers. Int. J. Solids Struct. 73–74, 99–112. http://dx.doi.org/10.1016/j.ijsolstr.2015.07.001.

Vardoulakis, I., Aifantis, E.C., 1994. On the role of microstructure in the behavior of soils: Effects of higher order gradients and internal inertia. Mech. Mater. 18 (2), 151–158. http://dx.doi.org/10.1016/0167-6636(94)00002-6.

Vesnitskii, A.I., Metrikin, A.V., 1996. Transition radiation in mechanics. Phys.-Usp. 39 (10), 983–1007.

Wazne, A., Reda, H., Ganghoffer, J.F., Lakiss, H., 2024. Nonlinear wave propagation in homogenized strain gradient 1D and 2d lattice materials: Applications to hexagonal and triangular networks. ZAMM Z. Angew. Math. Mech. 1–22. http://dx.doi.org/10.1002/zamm.202400426.

Zhang, J., Sulollari, E., Fărăgău, A.B., Pisanò, F., van der Male, P., Martinelli, M., Metrikine, A.V., van Dalen, K.N., 2021. Harmonic balance method for the stationary response of finite and semi-infinite nonlinear dissipative continua: Three canonical problems. Adv. Struct. Mater. 139, 255–274. http://dx.doi.org/10.1007/978-3-030-53006-8_16.

Zhou, S., Li, A., Wang, B., 2016. A reformulation of constitutive relations in the strain gradient elasticity theory for isotropic materials. Int. J. Solids Struct. 80, 28–37. http://dx.doi.org/10.1016/j.ijsolstr.2015.10.018.